CHAPTER 6

FINITE ELEMENT MODELLING

Finite element analysis (FEA) was applied to calculate the ruling parameters i.e. stress, strain and stress intensities for cracks in the shaft shown in figure 6.1. The theoretical aspects of fracture and numerical modelling were studied in detail. This chapter describes the different models used in the assessment.

A more detailed description of the turbine is given in chapter 1, but some aspects are repeated for the ease of reading. The rotors are of a typical dual flow LP turbine design with shrunk on blade carrier disks. Figure 6.1 shows a layout of the turbine construction used. The turbine has a shrunk on centre ring that is keyed to the shaft with 3 equally spaced axial keys as shown in figure 6.2. The disks are in turn keyed to the centre ring, and to each other, by axial drive pins. General industry consensus is that the cracks develop by fretting on the edges of the centre ring key, as depicted in figure 6.3. Figures 6.1 to 6.3 are repeated here (same as figures 1.1 to 1.3) for ease of reading.

The first attempts to analysis were led by work performed by the original equipment manufacturer (OEM), but calculation deficiencies were soon discovered. This work by the OEM was based on 2D analysis and assumed that the frictional stress resulting from the shrink fit of the disk is maintained during operation. This led to discrepancies between the results produced by the OEM and the first attempts by the author, who assumed that the frictional stress is released as a result of the cyclic strain produced on the surface of the rotor as a result of reverse bending during operation.

The following service loads were considered:

- Cyclic bending stress as a result of the rotor weight during rotation.
- Torque as a result of power generation through the different rotors in the train.
- Steady state stress as a result of the shrunk on disks.
- Frictional stress emanating from the shrink on process.

The following calculated values are required as inputs to fatigue and fracture assessment:

- ΔK_I Mode I stress intensity range as a result of bending
- K_I Mode I mean stress intensity resulting from shrink on and frictional stress.
- K_{III} Mode III stress intensity resulting from torque.
- R Stress ratio

Some, aspects like the influence of the frictional stress and the stress ratio, were investigated by 2D finite element analysis, which is also used as a measure to ensure convergence of 3D models. Simplified models were used to calculate different parameters after which the principle of superposition is used to assess the combined effects of the loads. General modelling considerations are discussed in the Appendix.

6.1. MODELLING CONSIDERATIONS

All models were constructed from the geometry provided in the OEM [U1] and manufacturing drawings. The area of interest is around the centre ring where the cracks are located (see figures 6.1 to 6.3).

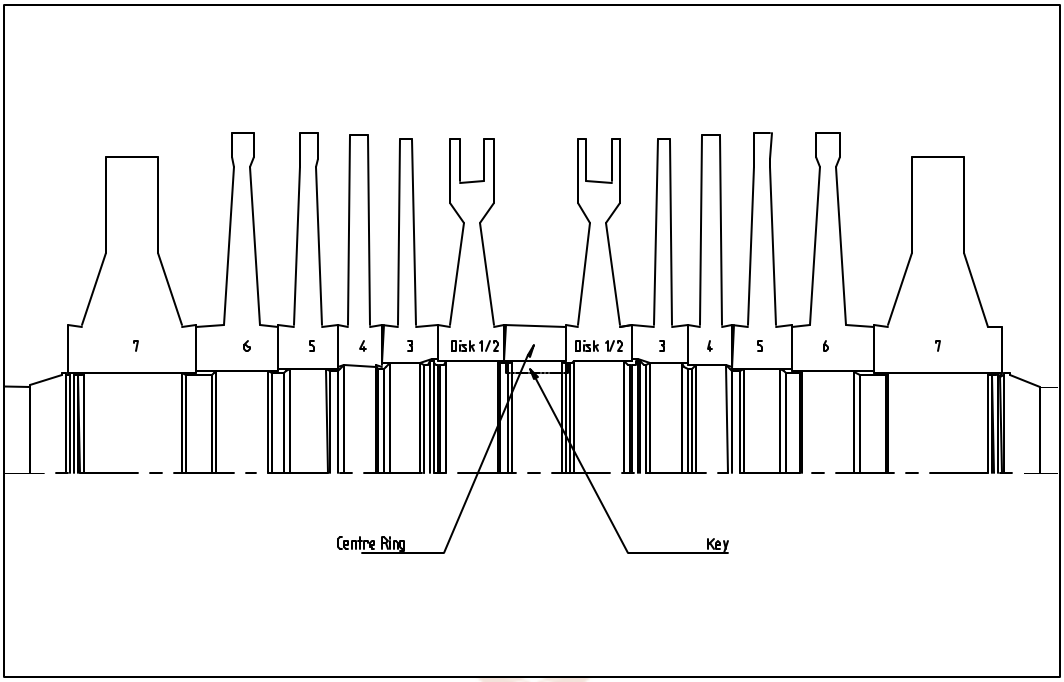

Figure 6.1: LP turbine layout

The material density was used as 7840 kg/m^3 in all models. The shrink fit of the centre ring and stage 1-2 disk was applied with interference as shown in table 6.1. The solid model boundaries of the shrink fit area were modelled with the interference in place i.e. overlapping.

Component	Shaft Diameter [mm]	Interference to apply at time of fitting [mm]		Interference applied for analysis. [mm]
		Max	Min	
Ring	967.6	1.000	0.940	0.990
Disk ½	960.0	2.280	2.220	2.225
Disk 3	940.0	1.560	1.500	1.560
Disk 4	920.0	1.820	1.760	1.820
Disk 5	900.0	1.760	1.700	1.760
Disk 6	880.0	1.760	1.704	1.760
Disk 7	860.0	1.900	1.844	1.900

Table 6.1: Table of interference fits (interference on diameter)

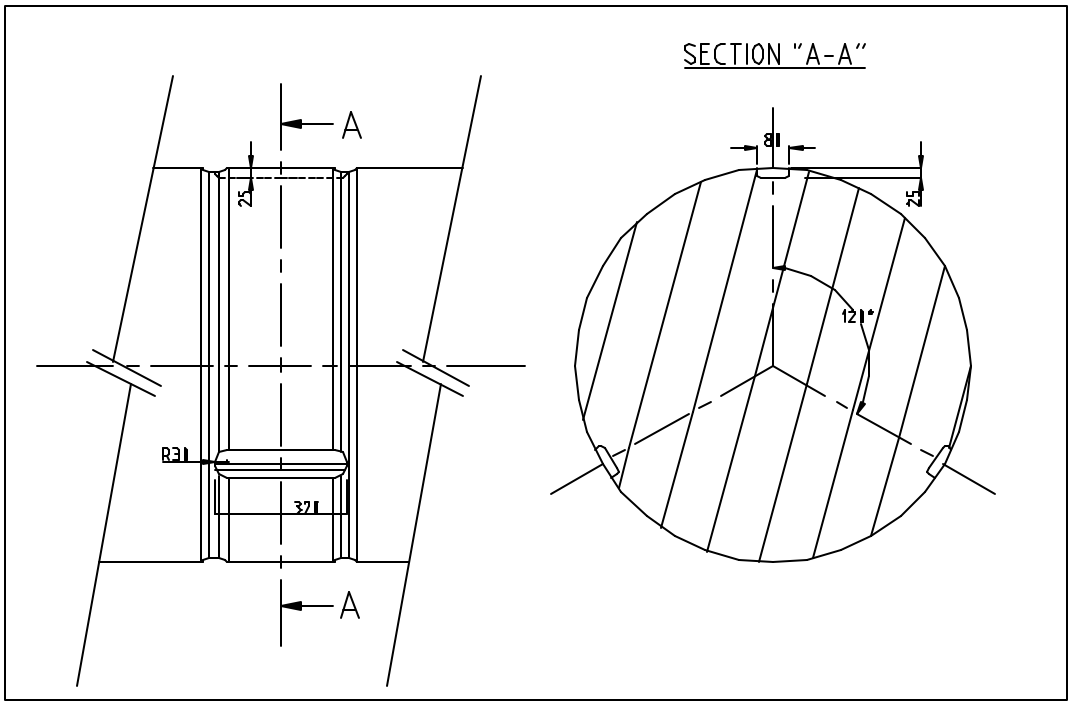

Figure 6.2: Details of key area (dimensions in mm)

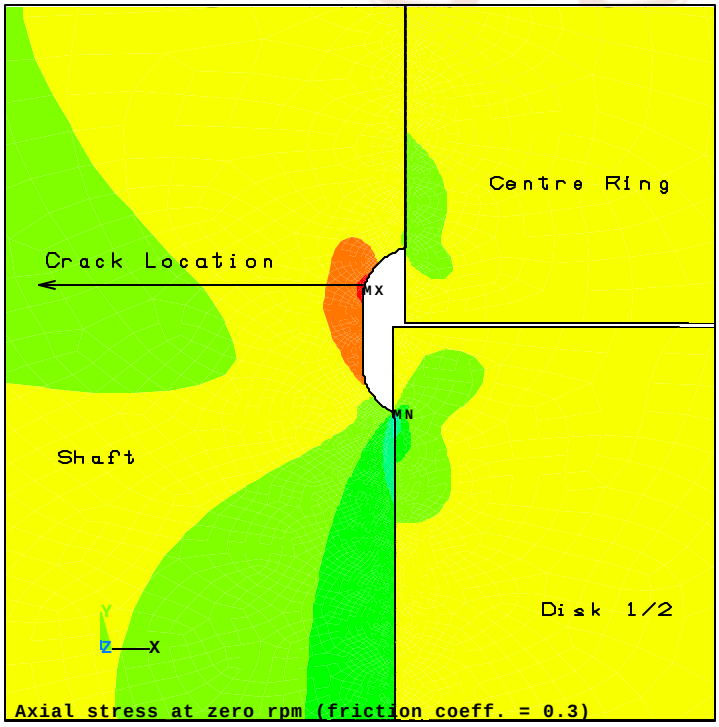

Figure 6.3: Crack Initiation Position (2-D) showing typical stress contours

In cases where friction was considered, contact elements were used at a coefficient of friction of 0.3 while constraint equations were used in cases where friction was neglected. Constraint equations are set up to enforce displacement compatibility in the radial direction such that the interference overlap is cancelled. For this purpose, exact overlapping mesh patterns are formed with one equation per corresponding node set. The advantage of this technique is that the non-linearity imposed by the contact problem is discarded together with the convergence difficulties of the curved surface. The concept is demonstrated in figure 6.4. Refer to Appendix for a general discussion on the FEA code and element types.

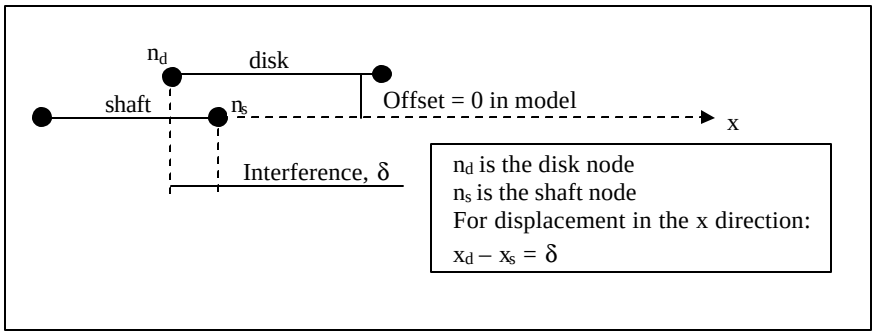

Figure 6.4. Constraint equation

A transverse cut through the middle of the rotor was used as a symmetry plane for all analyses. The assumption was made that a cut between disks 1/2 and disk 3 is also a symmetry plane, but that this plane is free to move in the axial direction as is the case for the actual rotor (see figure 6.1). The free end symmetry was modelled by coupling all nodes on this face in the axial direction i.e. the face is free to move axially but is forced to stay in the same plane. Figure 6.5. shows an axisymmetric presentation of the end constraints.

A bending moment of 1.2775 MN.m, equivalent to that caused by gravity, was applied over the section for the calculation of the bending stress and K_I amplitude (half the range). The bending moment was calculated from the available rotor geometry information and is not considered to be exact. It is, for example, not known what the weight-contribution of the couplings is and the geometry of the couplings are not available for verification. The assumptions for the bending moment are seen as conservatively realistic, considering the difference in rotor weights compared to the almost identical centre sections (section between bearings) [U1]. The bending moment of 1.2775 MN.m equates to a maximum bending stress of 15.67 MPa for a shaft radius of 0.47 m [U1].

The applied torque was calculated from the power distribution, at maximum power, between the rotors from the following information (see figure 6.6):

HP : 30 % = 298.5 MW
LP1,2,3 : 23.3 % = 3 x 225.2 MW or 112.6 MW per flow

The torque (K_{III}) acts as a retardation mechanism for crack growth, but increases the stress intensity for final fracture (see chapter 5). LP1 would have the smallest torque and should have the lowest threshold value for crack growth while LP3 would have the largest torque and the smallest critical crack size. Applied torque values of 2.618 and 5.487 MN.m were used for LP1 and LP3 respectively as calculated for the rotor centre. Refer to Appendix for the calculation.

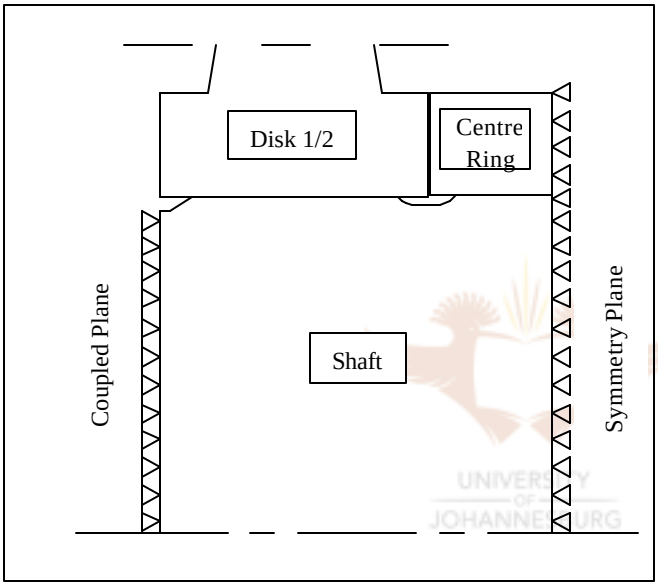

Figure 6.5: End constraints of model

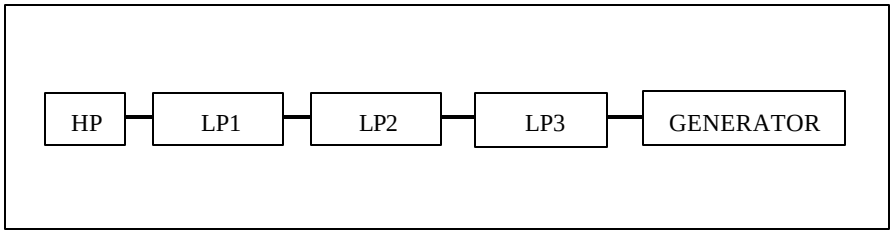

Figure 6.6: Generation train assembly

References P7 to P12 report that transverse cracks in rotating shafts develop into a crescent moon shape. A range of crack sizes was investigated. Crack shapes were chosen to resemble the crescent moon shape observed in the references. The cracks initiate from the key so that small cracks are likely to follow the key shape and have a

semicircular form. Figure 6.7. shows the cracks analysed, ranging in depth from 25 mm through 50, 100, 150 and up to 200 mm. An additional small crack of 5 mm on the key edge was investigated.

In a linear elastic analysis, the crack models used for the calculation of ΔK_I and K_{III} are not dependent on the disk shrink effects. For this purpose a shaft model is used with the same end constraints as in figure 6.5, but with a moment and torque applied to the nodes at the coupled end. The disk was omitted from this shaft model.

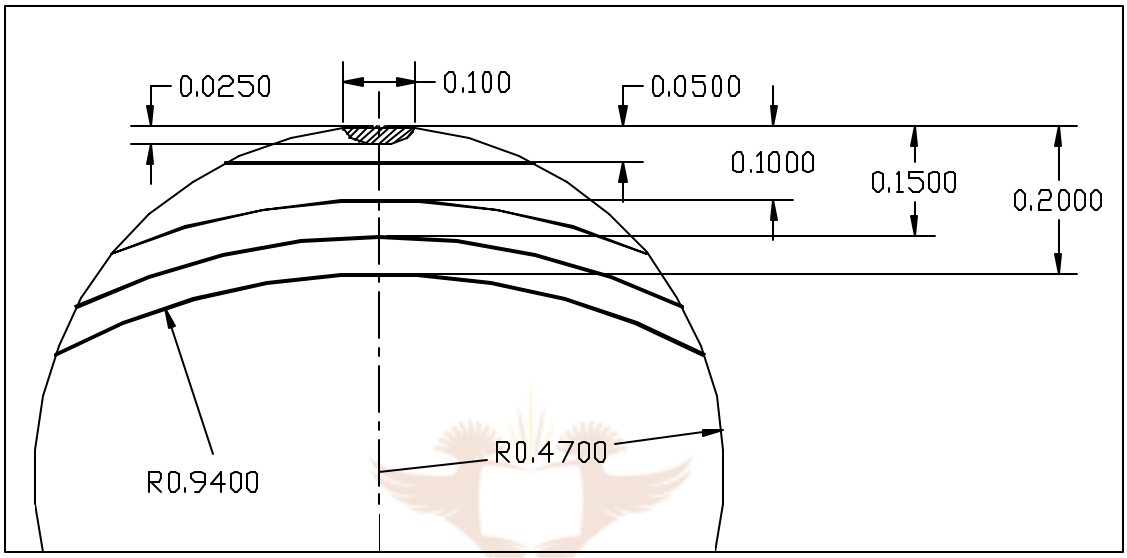

Figure 6.7: Crack shapes and sizes used for analysis (dimensions in m)

A 3D extension of the model in figure 6.5 was used with a crack to calculate K_I resulting from disk shrink effects. The blade mass results in a radial centrifugal force on the periphery of the disk. This force is speed dependent and the magnitude of the force was determined from the centre of gravity and the mass of the blade in accordance with equation 6.1.1. The centrifugal force was applied as a negative pressure over the area of the blade attachments.

$$F_c = m r_g \omega^2 \qquad (6.1.1)$$

where F_c = centrifugal force
m = blade mass
r_g = centre of gravity
ω = speed in radians per second

Numerical values of 15.1, 18.3 and 31.0 MPa were calculated for stages 1, 2 and 3 respectively at 1500 rpm.

6.2. 2D FINITE ELEMENT ANALYSIS

An analysis report was received from the OEM [U1]. The analysis was based on a 2D model and correlated the calculated stress values to known analytical stress intensities.

The assessment report of the OEM shows very little detail on the calculation of fracture parameters, but obvious shortfalls include:

- The analytical solution used for the calculation of ΔK_I is not for representative cracks.
- The stress solution for a crack free shaft was used. This would normally suffice for remote load influences, but proximity of the crack to the shrink fit area suggests that stress redistribution may take place in this case. This will have an influence on K_I and the stress ratio, R, which in turn influences the fatigue threshold.
- The effect of K_{III} is not accounted for.
- The calculated values do not support the actual behaviour of cracks observed in the turbines.

It was decided to duplicate the OEM's stress analysis as a first attempt towards ensuring the correct understanding of the influencing factors. This step was considered important to ensure that the correct assumptions are incorporated in a time consuming 3D analysis.

The axisymmetric model shown in figure 6.5 was used to obtain the first solution. The assumption was made that frictional stress releases during operation and needs not be considered. It was soon evident that there are major differences in the results compared to the OEM analysis. A range of solutions were obtained with variation in the boundary conditions and model assumptions (see table 6.2) in an attempt to explain the differences in results.

The OEM analysis reported axial stress-contours only at zero and 1500 rpm rotor speeds. Results were extracted for comparison to the OEM analysis and are displayed in table 6.2. None of the models could simulate the OEM analysis. The reason for this was that the OEM considered frictional stress at a coefficient of 0.3 as was discovered during discussions later on. Although not directly confirmed the OEM used symmetry boundary conditions at both ends of the rotor section. Since the rotor is free to move axially, a coupled plane on the one end would be more appropriate.

A 2D finite element solution was obtained for a case with friction, using the boundary conditions reflected in case 4 of table 6.2. Figure 6.1 shows a contour plot of the axial stress at 0 rpm for this solution. Results were extracted for the path along the crack location (as shown in figure 6.1) and are displayed in figure 6.8.

	1 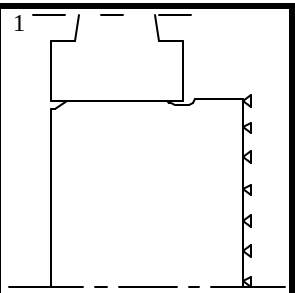		2 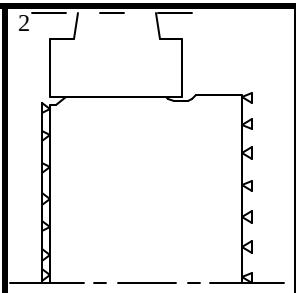		3 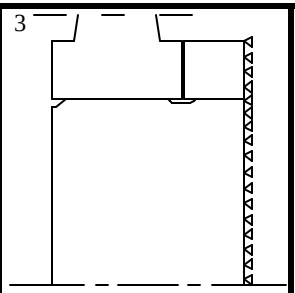		4 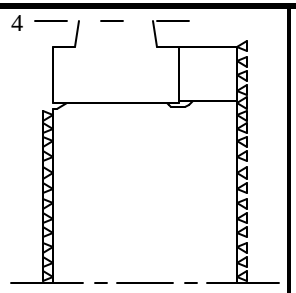		5 OEM	
	0 rpm	1500 rpm	0 rpm	1500 rpm	0 rpm	1500 rpm	0 rpm	1500 rpm	0 rpm	1500 rpm
σ_{ax}(max)	201	100	189	91	194	91	152	85	175	120
σ_{1st}(max)	203	116	190	91	196	92	153	85	-	-
σ_{ax}(Disk)	-51	-21	-61	-30	-46	-18	-53	-23	~ -100	~ -100

Table 6.2: Finite element results with values in MPa

Key to table 1:

σ_{ax}(max) : Maximum stress in the axial direction.
σ_{1st}(max) : Maximum 1st principal stress.
σ_{ax}(Disk) : Axial stress in the axial direction below the disk (approximately in the middle of the shrink fit area)

Coupled node set.

Symmetry boundary condition

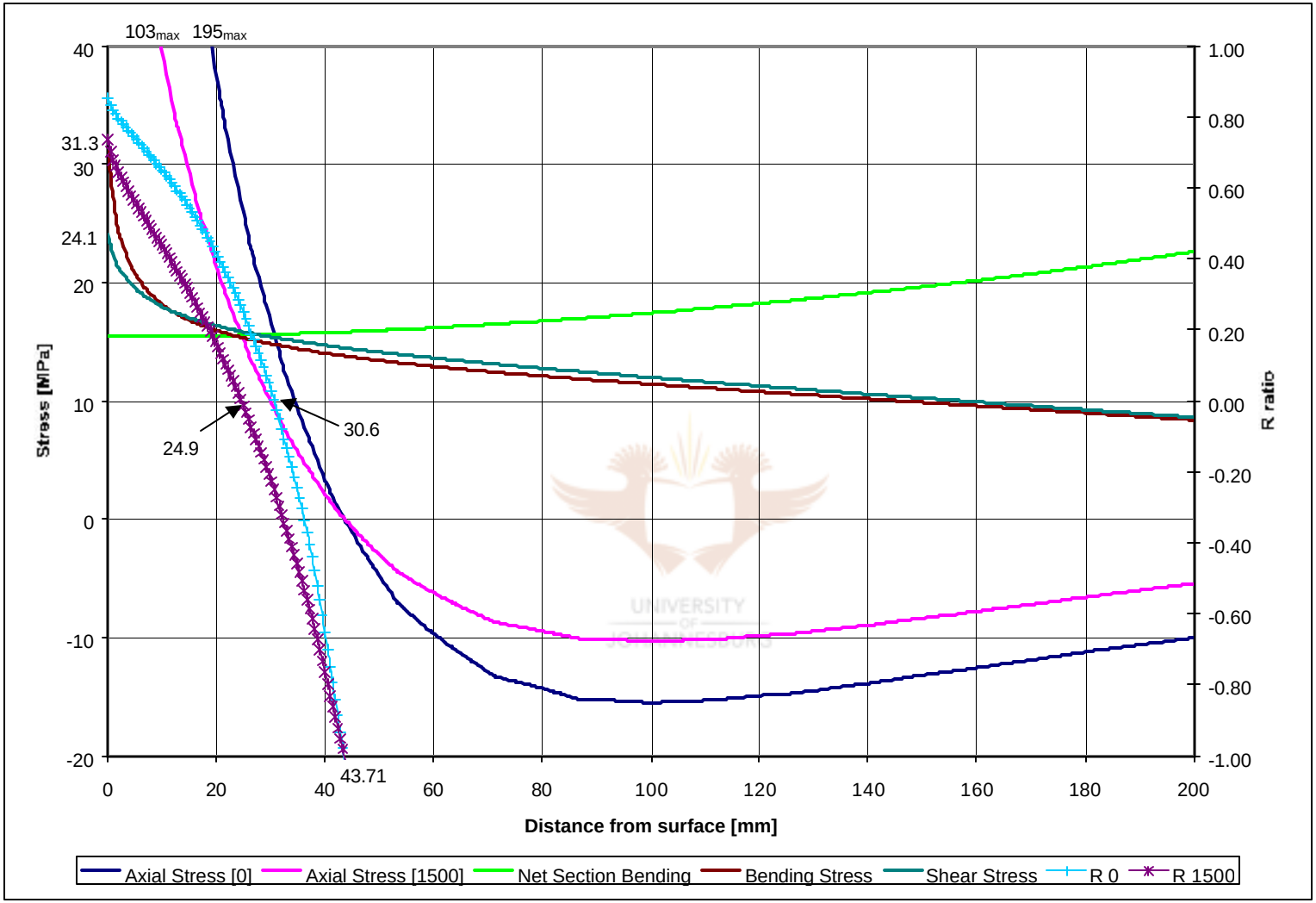

Figure 6.8: Axisymmetric stress results for a path along the crack location

The net section bending stress in figure 6.8 was calculated analytically (standard beam theory). The bending and shear stress was calculated by FEA through the use of harmonic elements that allow for the application of non axisymmetric loads. The stress ratio, R, is based on the crack free solution as calculated in the axisymmetric model.

The OEM[U1] used an analytical solution to derive ΔK_I as follows:

$$\Delta K_I = F\Delta\sigma\sqrt{\pi a} \qquad (6.2.1)$$

where F is a geometry factor and $\Delta\sigma$ is the cyclic bending stress range. A conservative estimate for F was extracted from a table in the OEM report as 0.7. The cyclic bending stress was reported earlier as 15.67 MPa for a range of approximately 32 MPa.

Figure 6.8 shows that an R ratio of –1 is reached at a depth of 43.7 mm for the 0 rpm solution. The fatigue threshold, $\Delta K_{I,th}$, can be calculated in accordance to equation 5.4.7 and is displayed with ΔK_I (as calculated by equation 6.2.1) in figure 6.9 for speeds of 0 and 1500 rpm. The fatigue threshold was only adjusted for stress ratios down to –1 after which it was held constant. In reality the effective ΔK_I would reduce further (equation 5.4.3), resulting in further increases in $\Delta K_{I,th}$ according to the trend in figure 6.9.

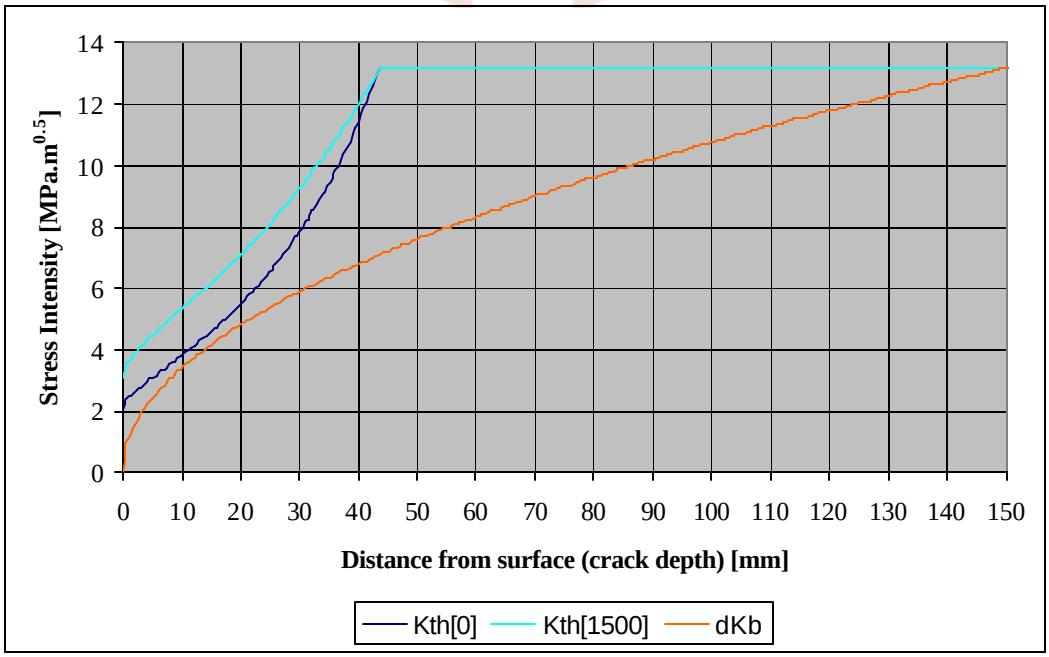

Figure 6.9: Crack parameters from axisymmetric analysis

The result shows that no crack growth is possible beyond the influence of the stress raising effect of the relieve are (recess between the centre ring and disk 1/2), because the applied stress intensity range, ΔK_I, is always smaller than the fatigue threshold, $\Delta K_{I,th}$. Figure 6.8 shows the increase in stress over the first 10 mm as a result of stress concentration. Equation 6.2.1 does not hold true in the stress field surrounding a stress concentration.

The result of this analysis does not reflect industry experience. The 2D analysis needs to be expanded to include more accurate calculation of 3D crack models, the effect of K_{III} and the influence of friction must be investigated.

6.3. FRICTION

The basis for the initial assumption that frictional stress can be neglected stems from the following argument:

Frictional stress results from the relative movement between the shaft and disk during cooling down period following the shrink fit operation. Subsequent operation of the turbine can result in further relative movement that may see release or reversal of the frictional stress. It is also possible that the frictional stress release due to incremental movement caused by alternating bending stress.

Figure 6.10 shows a schematic presentation of the progression. Figure 6.10.a represents the initial shrink fit. The frictional forces, F_f, result in a tensile stress in the relieve area, adjacent to the shrink area.

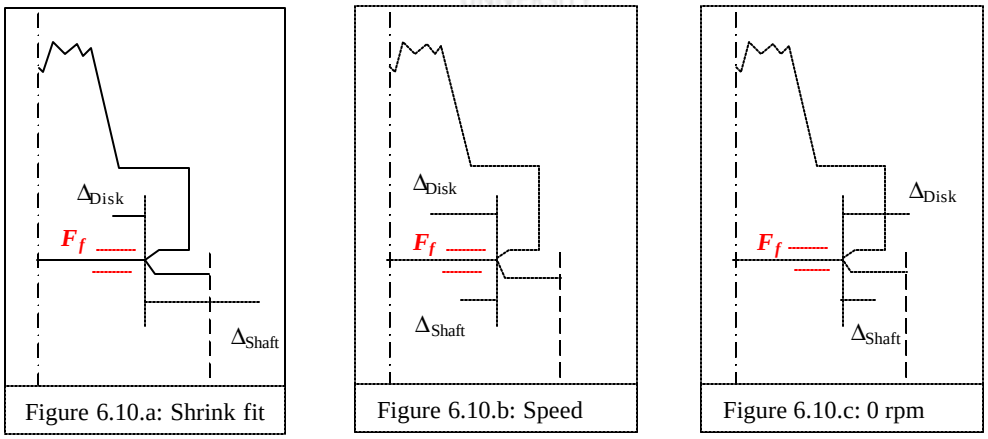

Figure 6.10.a: Shrink fit | Figure 6.10.b: Speed | Figure 6.10.c: 0 rpm

Figure 6.10: Frictional stress in assembly

When the rotor spins up, the relative movement increases and maintains the frictional force direction as shown in figure 6.10.b. When the rotor spins down from speed, the relative movement causes a frictional force in the opposite direction, figure 6.10.c.

The movement in figure 6.10.c may result in relieve of the initial frictional force or a frictional force in the opposite direction, depending on the amount of movement.

A rotor that is similar in design (shrunk on disks) was stripped for maintenance purposes (see figure 6.11). The rotor has a smaller diameter and operates at a higher speed of 3000 rpm compared to 1500 rpm in the case study.

A strain gauge was attached to the shaft using an epoxy adhesive that would allow the gauge to withstand 220°C. The disk was heated to a much higher temperature when it was shrunk on, but is not in direct contact with the gauge. The gauge was located 65 mm from the landing of disk four, as shown in figure 6.12.

Measurements were taken from the gauge before and after disk four was installed using the DMD20A amplifier. Once the rotor had been transferred to the balancing pit a telemetry system was connected to the gauge to measure the change when the turbine was run up to normal operating speed. The overspeed condition was also monitored. Due to costs, telemetry tests had to be performed in parallel to rotor balance activities so that the speed could not be explicitly controlled for measurement purposes.

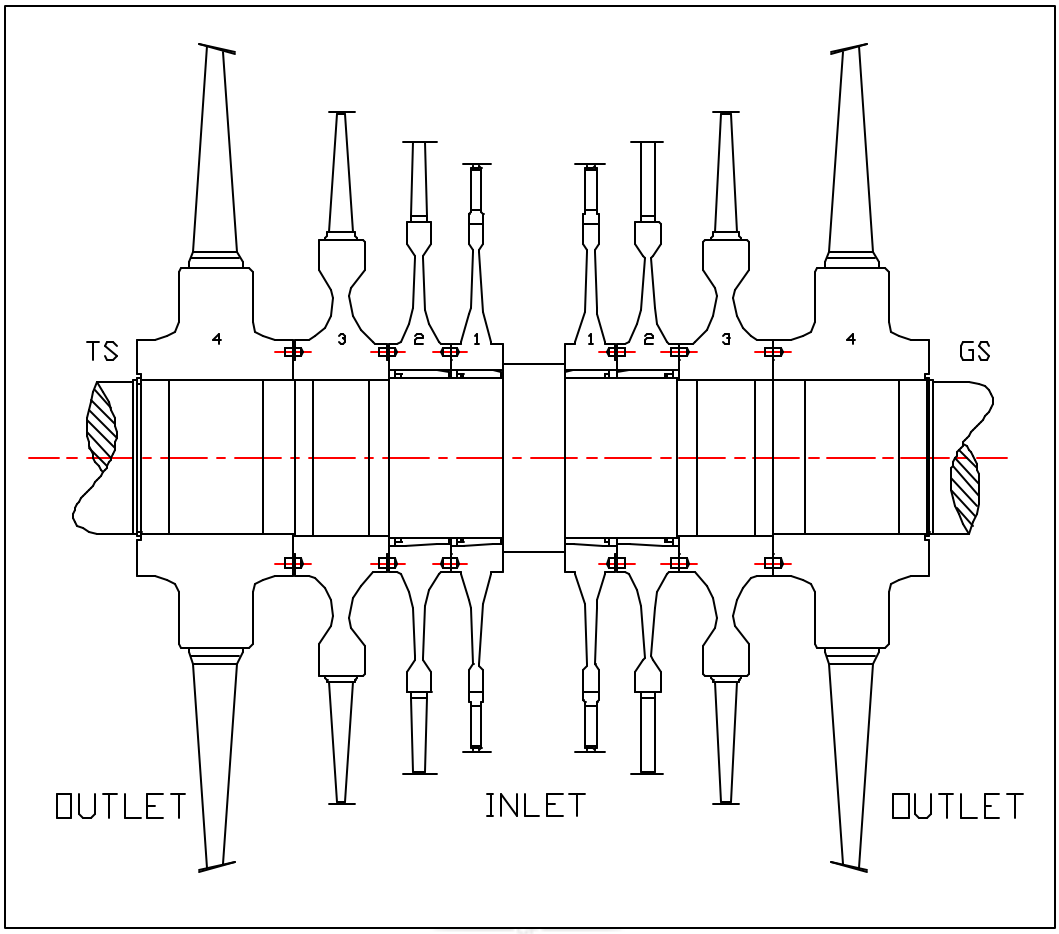

Figure 6.11: Turbine used for friction measurements

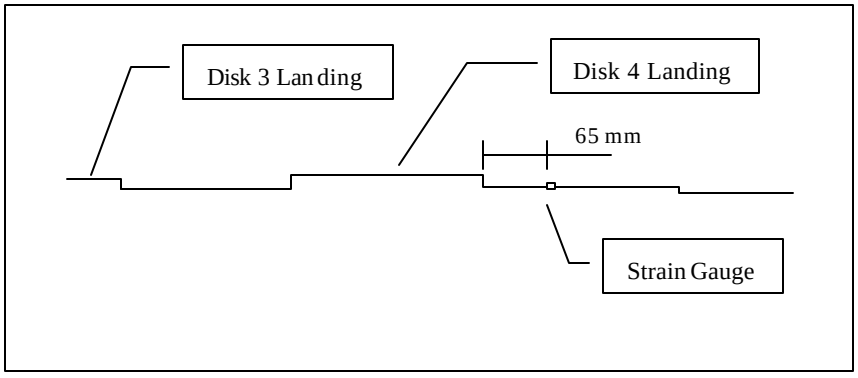

Figure 6.12: Schematic of Strain Gauge Position

The strain induced during the fitting of disk four was 329 µm/m. A decrease in this strain would indicate release, or reversal in direction, of frictional stress.

The results of the telemetry tests are shown in table 6.3. The strain was set to a reference of zero at a speed of 0 rpm for the telemetry testing. This means that a strain of zero in table 6.3 is equivalent to the initial strain of 329 µm/m that was invoked during the shrink process.

The strain in the shaft varied according to the speed of the shaft as expected. This variation is made up of two components namely:

- Strain change as a result of centrifugal lifting of the disk relative to the shaft (release of interference fit).
- Changes resulting from friction release from the initial shrink on condition.

The first run up to 3000 rpm showed a non linear change in strain as a function of speed as shown in figure 6.13. The non linear behaviour is expected because of the cubic relationship of centrifugal force as a function of speed (see equation 6.1.1). At 3000 rpm, there was a further shift in strain at constant speed. The rotor was then cycled between 3000 and 400 rpm for a number of times.

Measurements could only be taken at 400 and 3000 rpm for this period. The results showed that the stain change for this operation was linear elastic in nature i.e. the strain at 400 and 3000 rpm had the same values for consecutive cycles. Comparing values at 400 rpm between the first run-up and consecutive cycles showed a permanent strain change of –49.5 – (–6) = –43.5 µm/m.

TELEMETRY MEASUREMENTS			
FIRST RUN UP TO 3000 rpm		OVERSPEED RUN TO 3450 rpm	
SPEED [rpm]	STRAIN [µm/m]	SPEED [rpm]	STRAIN [µm/m]
0	0.0	0	-42.3
400	-6.0	400	-49.5
1020	-33.8	1020	-76.1
1500	-71.3	1500	-114.7
1980	-118.4	1980	-164.3
2520	-198.1	2520	-234.3
3000	-309.2	3000	-303.1
3000	-312.8	3450	-417.9
3000	-316.4	3450	-421.5
400	-49.5	3450	-421.5
		400	-103.9
Permanent change	-43.5		-54.3
TOTAL CHANGE			**-97.8**

Table 6.3: Telemetry results of friction experiments

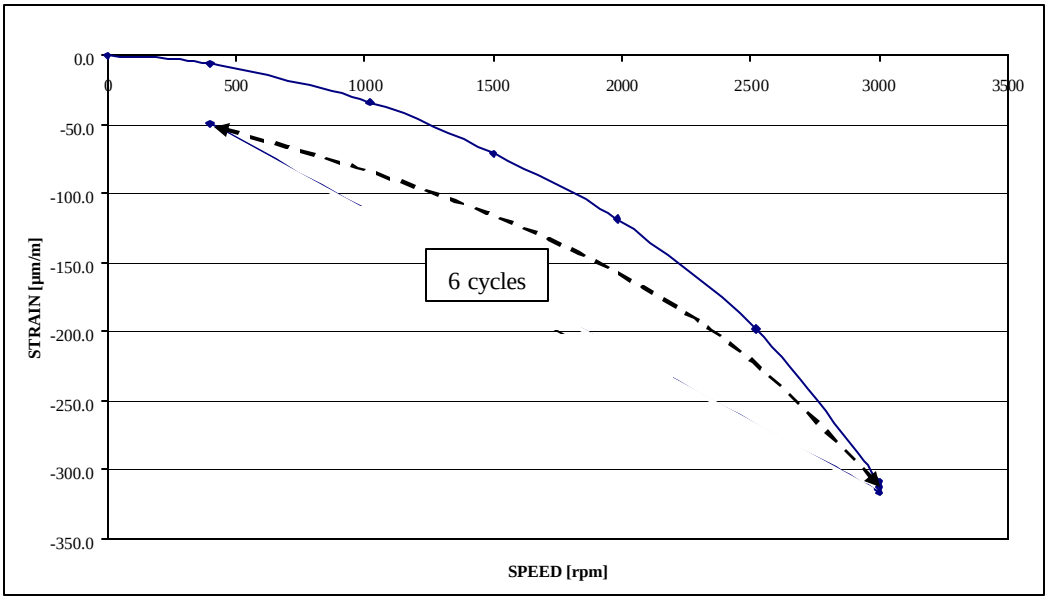

Figure 6.13: Strain measurements for run-up to 3000 rpm

When the turbine was run up to the overspeed condition of 3450 rpm there was again a permanent shift in the strain reading, this time it moved –54,3 µm/m. The behaviour was again elastic after this shift (see figure 6.14).

The total permanent shift in the strain reading was –97.8 µm/m.

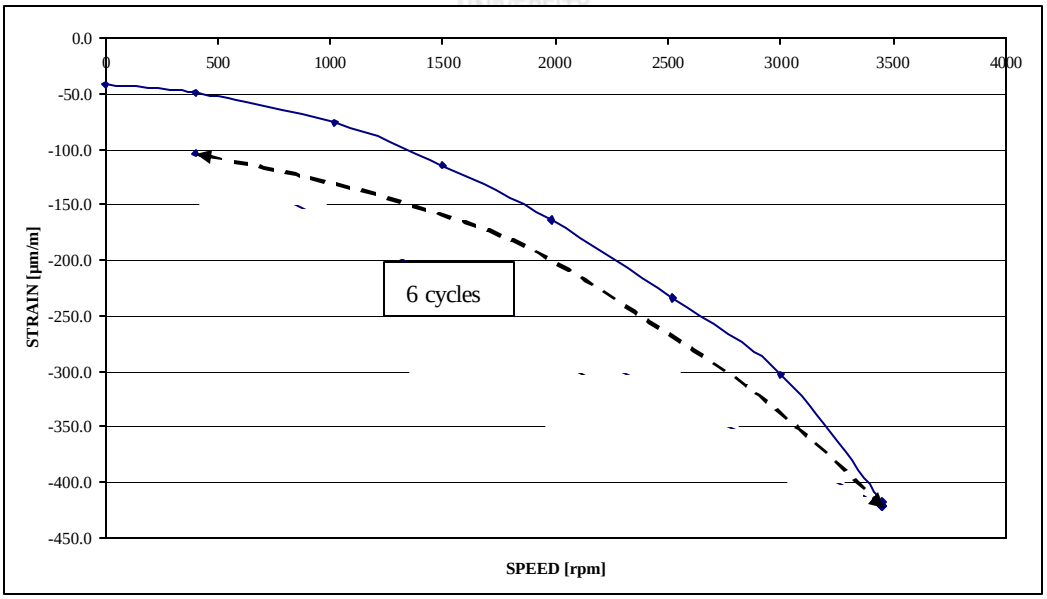

Figure 6.14: Strain measurements for overspeed tests

Finite element analysis was performed on shaft to calculate the different strain components (shrink and friction) for comparison with the measured results. Figure 6.15 shows the geometry that was used. Eight node quadratic elements were used in an axisymmetric finite element formulation. The blue triangles along the upper boundary indicate a symmetry plane, while the green triangles along the lower boundary indicate a coupled plane.

The coupled plane is allowed to move vertically, but all nodes are forced to stay in the plane as it would be constrained by the remaining section of the rotor. Disk three was included in the model to eliminate boundary effects on the symmetry plane side of the model.

The red triangles show the constraint equations for the symmetry plane. Two different models were used on the shrink interface namely contact elements and constraint equations. Friction forces cannot be transmitted in the constraint equation model, but the formulation allows for rapid evaluation as discussed earlier.

Key	Previous	Method	RPM	Friction
C1		Constraint equations	0	0
C2	C1	Constraint equations	3000	0
F1		Contact elements	0	0.3
F2	F1	Contact elements	3000	0.3
F3	F2	Contact elements	0	0.3

Table 6.3: Key to load cases solved

Table 6.4 gives a key to the load cases. The centrifugal blade forces were applied as pressures on the disk rim where applicable, as was done for the case study.

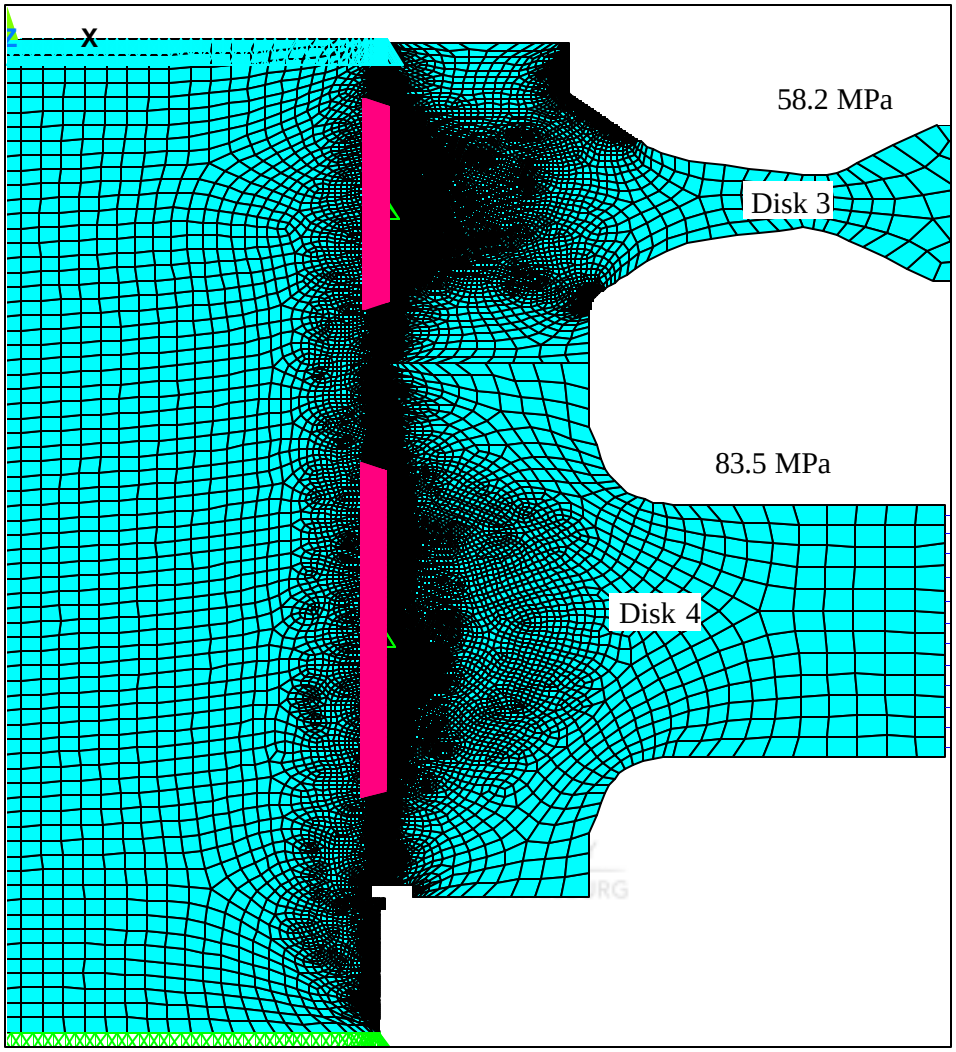

Figure 6.15: Finite element model for frictional stress analysis

Results were extracted along the face on which the strain gauge was glued (see figure 6.12). The results are presented in figure 6.16 with the horizontal axis measured from the edge of the disk 4 landing i.e. the 65 mm offset point on the graph represents the position of the strain gauge. The figure shows that the frictionless result at 0 rpm, C1, is closely approximated by the friction result at 0 rpm, F3, after one cycle.

Table 6.4 shows the analysis results compared to the measured results. The measured values are derived from the measured results taking account of the fact that the measurements were zeroed before telemetry testing. The initial shrink fit strain should be evaluated against the F1 load case. The strain gradient in the vicinity of the gauge is approximately 10 μ-strain/mm according to the finite element analysis. The finite

element result (396 μ-strain) differs from the measured result (329 μ strain) by 67 μ-strain.

The finite element result is the same as the measured result at a location 7 mm further away from the shrink fit edge. There is a small radiused transition from the shrink fit to the landing on which the strain gauge was attached. The radius may have had some influence on the accuracy of the placement of the strain gauge. There is also a possibility that the strain gauge behaviour may not have been influenced by the initial temperature cycle of the shrink process. The gauge performance was however checked afterwards and found satisfactory.

Method	C1	C2	F1	F2	F3
FEA	319	42	396	76	323
Measured	-	-	329	329-316.4	329-43
	-	-		=12.6	=286
Difference	-	-	67	64	37

Table 6.4: Finite element results for frictional analysis

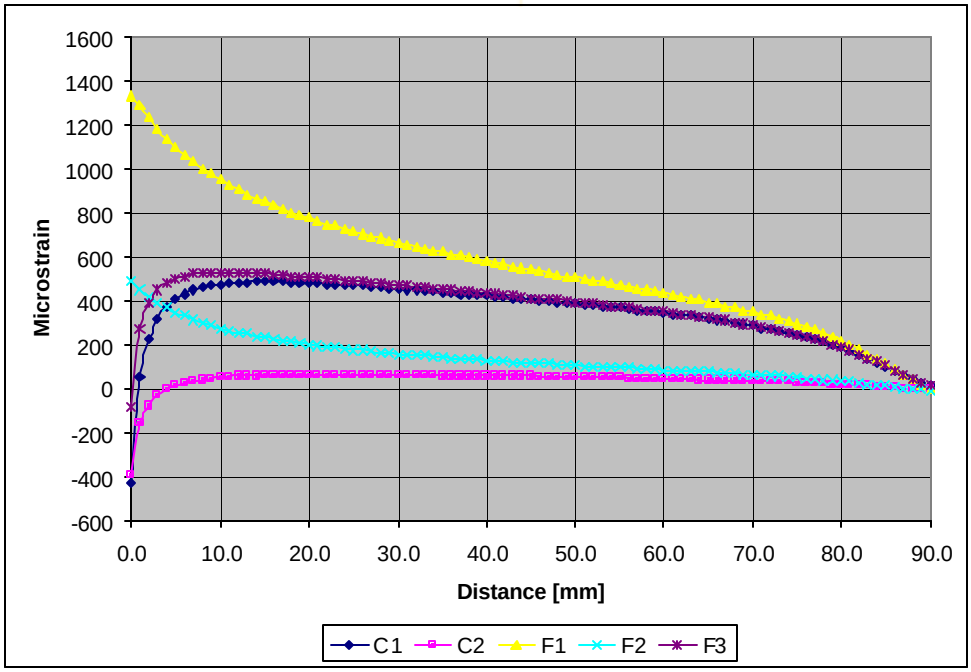

Figure 6.16: Strain profiles for the load cases considered

The difference between cases C1 and F1 shows the total available frictional strain that can be released by dynamic effects and relative movement, assuming that the actual friction coefficient is 0.3. The OEM reported that a friction coefficient of 0.2 to 0.3

was verified by experimental results for shrunk on disks [U1]. General text book references, example reference T16, show that in the absence of lubricants, the higher value of 0.3 is more likely. The total range is 396 – 319 = 77 μ-strain. The measured results show that 43.5 μ-strain released for the equilibrium condition between 0 and 3000 rpm compared to the available 77 μ-strain calculated by FEA (difference between F1 and F3). It is possible that the difference of 33.5 μ-strain (77 – 43.5) is absorbed elastically.

Table 6.4 shows that cases F1 and F2 have approximately the same difference compared to the measured results. This may indicate that the initial difference is not real and that it may be a result of the factors discussed earlier.

The difference in the F3 result probably shows that the dynamic behaviour of the shrink fit is not accurately modelled. Three factors were identified as potential contributors to the difference in calculated and measured results namely:

- Actual friction coefficients and dynamic effects in the transition between static and sliding friction.
- Cyclic dynamic effects are not accounted for in the analysis and may play a significant role in the actual behaviour of the shrink fit. Load cases C1 and F1 would not be influenced by the dynamic effects.
- The analysis assumed rigid coulomb friction. No references could be found on the quantitative behaviour of elastic Coulomb friction for steel on steel. Figure 6.17 demonstrates the difference between rigid and elastic friction.

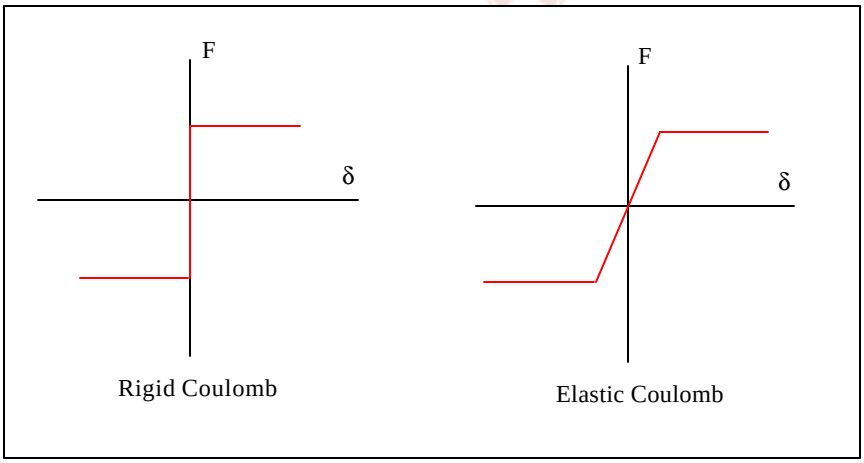

Figure 6.17: Friction models
F=Friction force
δ=Relative movement

A number of attempts were made, without success, to get a model with better correlation to the measured results by varying elastic Coulomb stiffness, load ratte etc.. Modelling of friction-contact problems is complex and computing intensive.

More gradual loading and load variation should also improve the reliability of results. Load rates are important because energy lost in sliding cannot be recovered in the numerical models.

The overspeed case was not modelled, but the measured results show a total strain release of 97.8 μ-strain compared to the calculated available 77. This means that the direction of the frictional forces were reversed to work in a direction that will result in compressive stress in the strain gauge area (see figure 6.10.c).

This section is concluded by the following argument (neglecting potential modelling inaccuracies):

- Initial cycling to 3000 rpm has shown that the shrink fit has the property that it can absorb a strain of 32.5 μ-strain out of the 77 μ-strain available in an elastic mode.
- If the turbine is subjected to an overspeed test so that the direction of the frictional stress is reversed, it should also be able to elastically absorb a strain of 32.5 μ-strain in the other direction. The expected total strain change would then be 77 + 32.5=109.5 μ-strain. This value compares well with the 97.8 μ-strain measured.
- The analysis for the case study does not include an overspeed cycle, but merely release the friction strain from the initial shrink fit. This means that frictional force in the case study would be conservative i.e. 77 μ-strain calculated vs. 97.8 measured in the experiment.

6.4. 3D FINITE ELEMENT ANALYSIS

3D Finite element calculations are divided into two categories for the purpose of this work. They are:

- Calculation of parameters related to shrink and frictional stress. K_I falls in this category. A full 3D model with the disk and centre ring with the interference interface is used in this analysis.
- Calculation of parameters related to bending and torsion. A simple shaft model is used for this purpose. The model includes the key geometry, but the disk and centre ring is omitted. ΔK_I and K_{III} fall in this category.

Both categories use a crack front model with quarter node wedge elements as discussed in chapter 4. The principles investigated in chapter 4 were used, together with limited mesh refinement studies, to ensure convergence. The 6.18 shows the finite element mesh for the 25 mm deep crack (see figure 6.7).

The shrink fit was modelled by contact elements to enable friction on the interface. Frictional effects were investigated in a 3D model to confirm the conclusion derived in the 2D analysis and to compare the result with the case of friction release.

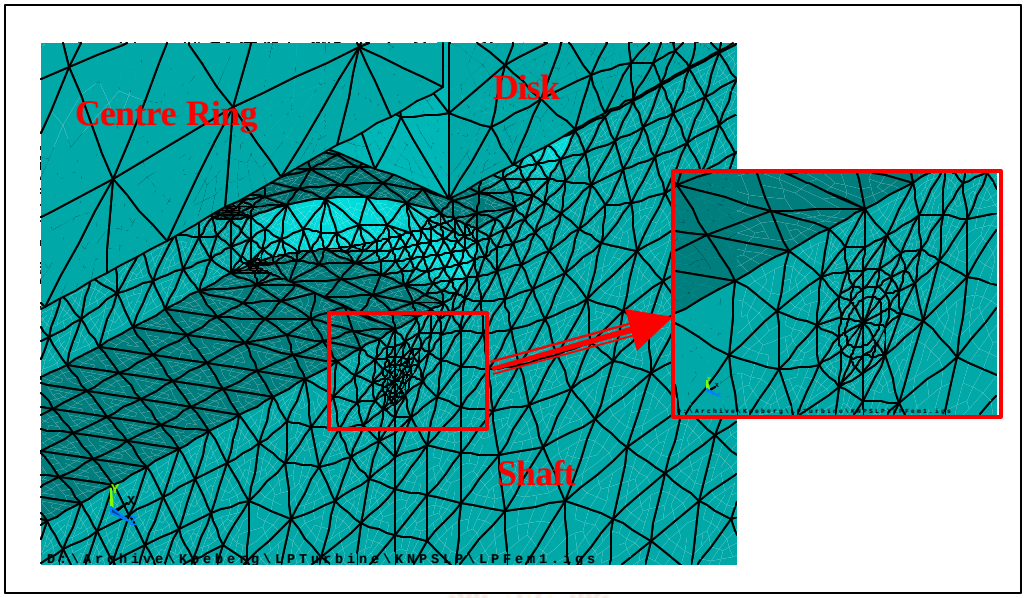

Figure 6.18: Finite element mesh for 25 mm crack

Multiple solutions were obtained for each model through chronological load steps as follows:

- solution at 0 rpm with friction
- solution at 1500 rpm with friction
- solution with friction release at 1500 rpm
- solution at 0 rpm with friction reinstated from previous load step (1500 rpm)

Table 6.5 shows the calculated results. The key to the table indicates that the models for the larger cracks do not include the key geometry. The reason for this is that the crack tip stress for large cracks are outside the stress concentration effect of the key and the inclusion of the key results in a larger model (in terms of degrees of freedom) which takes longer to solve.

Crack Size [mm]	K_I **MPa.m^{½} [0 rpm]	K_I **MPa.m^{½} [1500 rpm]	K_{III} [1500 rpm] MPa.m^{½}			$\Delta K_I/2$ Bending MPa.m^{½}
			LP 1	LP 2	LP 3	
5	16.0 – 12.0	8.84 – 4.70	***	***	***	1.8
25	9.50 – 6.70	6.20 – 3.00	*4.1	*6.3	*8.5	3.3
50	8.60 – 4.40	4.40 – 0.43	*7.8	*12.0	*16.3	5.7
100	2.60 – 1.10	2.00 – 0.42	*11.3	*17.4	*23.6	*8.3
150	-	-	*13.4	*20.7	*28.0	*11.0
200	-	-	*15.4	*23.9	*32.3	*13.4

Table 6.5: Finite element results of fracture parameters for the case study

* - Calculated from shaft model without key.
** - Range shows the release in mean stress intensity under the assumption that the friction forces are released when the rotor goes through the critical speed (lower values are with friction release).
*** - K_{III} not calculated because the 5 mm crack is shielded from torsion by the key (see figure 6.19)

Figure 6.19 shows the axial stress distribution for a 5 mm crack on the lip of the key.

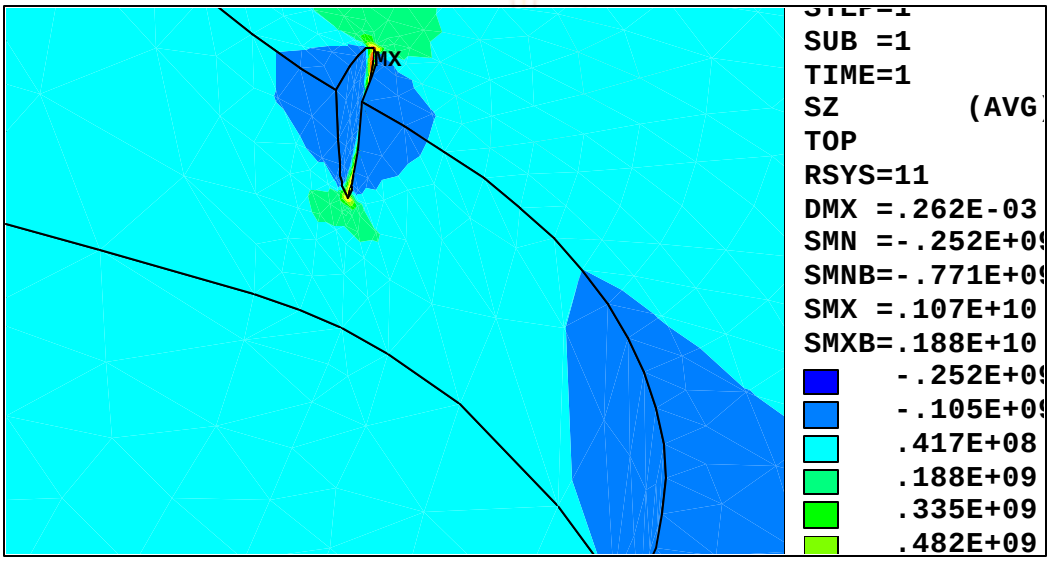

Figure 6.19: Axial stress distribution of 5 mm crack model (displacement scaling is enlarged)

Crack interaction was investigated by considering three 100 mm cracks i.e. one at each key (see figure 6.2). The solutions show an insignificant change in ΔK_I and K_I, but an increase by a factor of 2.14 in K_{III}. The mode 3 stress intensity, K_{III}, for LP3 would increase from 23.6 to 50.5 MPa.m$^{0.5}$ if three 100 mm cracks are present compared to one.

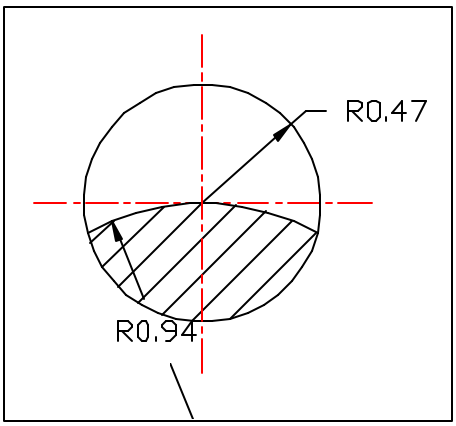

Figure 6.20: Shape of large crack

An additional crack was analysed to investigate the fracture for a crack extending halfway through the rotor. Figure 6.19 shows the shape of the crack. The convergence behaviour was investigated as a further test to the principles outlined in chapter 4. Three models were used for the calculation of ΔK_I.

The first attempt, figure 6.20, was to get a fine converged mesh. It was shown in chapter 4 that a small first segment requires small surrounding segments to be able to follow the steep strain gradients around the crack front. The second attempt, figure 6.21, was to get a coarse converged mesh with reduced computing time. The remote strain distribution in bending is linear and the finite element mesh does not need to be fine for convergence. A third mesh was solved with the optimised conditions of the 1st segment and 2nd segment at 0.1a with a as the crack depth.

The three models show good correlation and values of 29.70, 29.68 and 29.66 MPa.m$^{0.5}$ was recorded. The stress intensity range was calculated as 2x29.7= 59.4 MPa.m$^{0.5}$. K_{III} was calculated as 38.9 MPa.m$^{0.5}$.

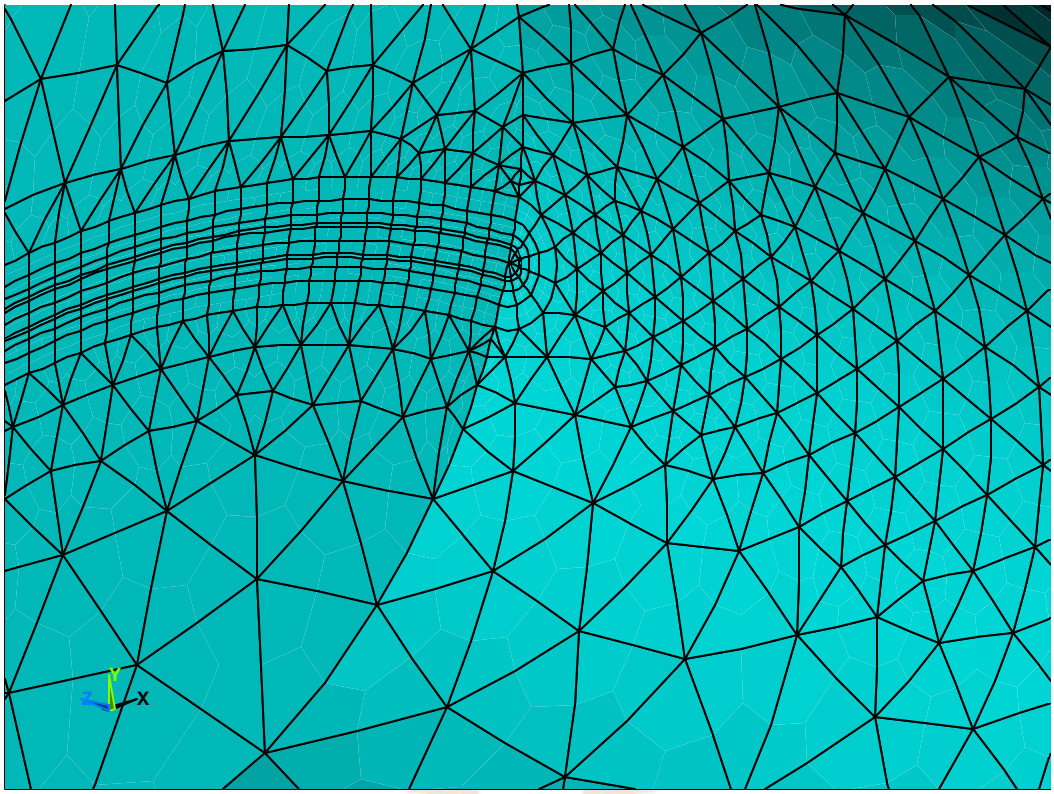

Figure 6.20: Fine mesh with 1st segment = 0.0213a, 2nd segment = 0.0064a, 3rd segment = 0.0149a; 4th segment = 0.0213a, 5th segment = 0.0632a (total of 0.1a in controlled mesh); remainder in free tetrahedron mesh; 21826 elements; 101827 degrees of freedom: K = 29.70 MPa.m$^{0.5}$ (a = crack depth = 0.47 m for the shaft).

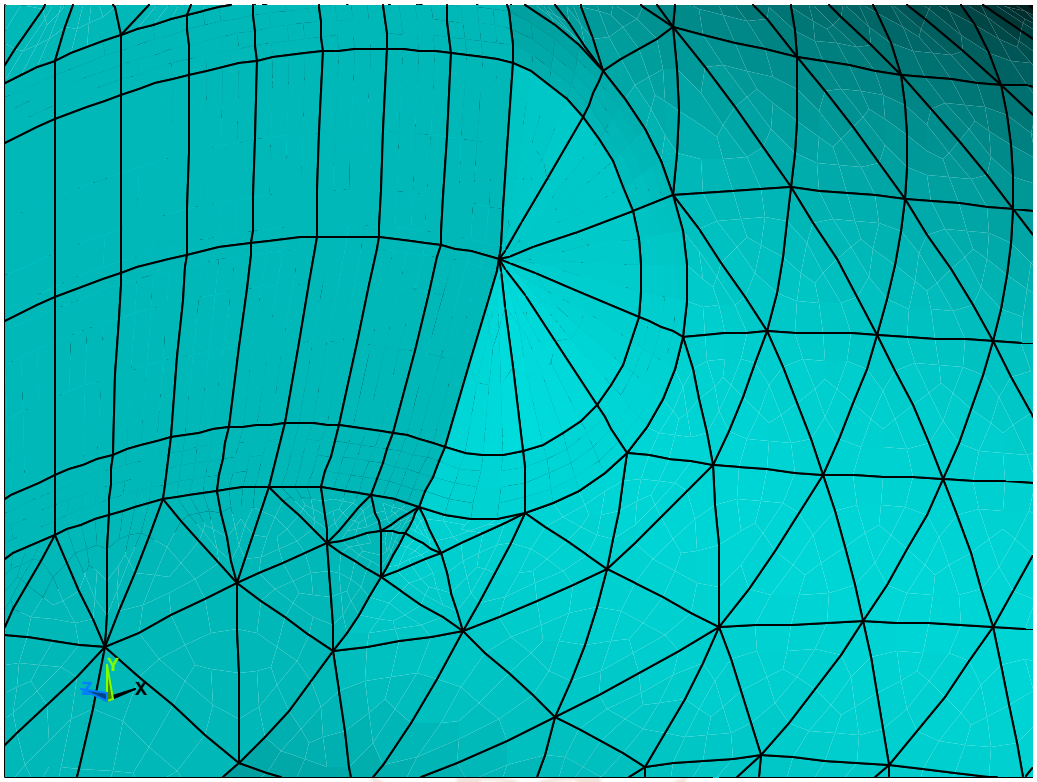

Figure 6.21: Coarse mesh with 1st segment = 0.4a, 2nd segment = 0.1a; remainder in free tetrahedron mesh; 4843 elements; 22880 degrees of freedom: K = 29.68 MPa.m$^{0.5}$ (a = crack depth = 0.47 m for the shaft).

6.5. CONCLUSIONS

The following conclusions are made:

- A 2D axi-symmetric finite element model does not describe the ruling parameters for fatigue and fracture assessment to sufficient accuracy.
- The influence of frictional stress was investigated by experiments and analysis and it was found that the friction is released by the dynamic fluctuations that take place when the rotor is in operation.
- The applied fracture parameters that are required for fatigue and fracture assessment were calculated and are reported in this chapter.